Dalton Transactions

ROYAL SOCIETY OF CHEMISTRY

PAPER

View Article Online
View Journal | View Issue

Open Access Article. Published on 11 August 2023. Downloaded on 3/9/2026 9:36:11 AM.
This article is licensed under a Creative Commons Attribution-NonCommercial 3.0 Unported Licence.

Check for updates

Cite this: *Dalton Trans.*, 2023, **52**, 12496

Investigation of the unique magnetic behaviours of isomers in a 1,2-dithiooxalato-bridged diiron(II) complex†

Takuya Kanetomo, *[a] Koki Yokoyama,[a] Yudai Suzuki,[a] Hiromichi Ida,[a] Atsushi Okazawa[b] and Masaya Enomoto *[a]

Received 27th June 2023,
Accepted 10th August 2023

DOI: 10.1039/d3dt01992f

rsc.li/dalton

1,2-Dithiooxalate (dto) can be employed as a bridging ligand and it exhibits symmetric (*O*,*S*-chelation) or asymmetric (*O*,*O*- and *S*,*S*-chelation) coordination forms. In this study, we prepared a novel dto-bridged diiron(II) complex, $[\{Fe(TPA)\}_2(\mu\text{-dto})](ClO_4)_2$ (**1**), where TPA is tris(2-pyridylmethyl)amine. Interestingly, the bridging dto ligand exhibited not only the asymmetric form but also a linkage isomer and a diastereomer within the same crystal. Notably, the three isomers of **1** exhibited different magnetic properties, resulting in a multi-step spin crossover behaviour.

Introduction

1,2-Dithiooxalate (dto, $C_2O_2S_2$) has *O*,*O*,*S*,*S*-donor atoms and can adopt various coordination forms. For instance, it can exhibit *O*,*O*- and *S*,*S*-chelation forms or two *O*,*S*-chelation forms, as illustrated in Fig. 1a and b, respectively. Note that the two configurations depicted in Fig. 1a and b are denoted in this paper as asymmetric and symmetric configurations, respectively, based on the centrosymmetry of dto. The choice of coordinating donor atoms to a metal centre is determined by the hard and soft acids and bases (HSAB) rule.[1] In the case of heteronuclear metal complexes, asymmetric coordination environments are commonly observed (Fig. 1a).[2–23] This arrangement often leads to desirable physical properties such as ferromagnetism,[11–13] single-molecule magnets (SMMs),[14] charge-transfer (CT) phase transition[15–21] and ferroelectrics.[22] On the other hand, the studies of homonuclear complexes with dto are relatively rare. For example, $[\{Ni^{II}(en)_2\}Ni^{II}(dto)_2]$ (en = ethylenediamine) exhibits an asymmetric configuration (Fig. 1a),[24] while homonuclear complexes of indium(III), silver (I) and zirconium(IV) with dto exhibit the symmetric configuration of dto (Fig. 1b).[25–27]

An iron(II) ion with a $3d^6$ electron configuration in an octahedral environment can exhibit two spin states, namely high-spin (*hs*, $S = 2$) and low-spin (*ls*, $S = 0$) states. These spin states depend on the coordination field in the presence of an appropriate ligand field. There is a spin transition between the *hs* and *ls* states triggered by external stimuli. This phenomenon is called a spin crossover (SCO).[28–32] It has been intensively studied using similar 3d-transition metal complexes such as iron(III),[33–35] cobalt(II)[36–40] and manganese(III) ions.[41,42] SCO materials have garnered significant attention and investigation due to their potential applications: for example, building blocks for switchable coordination polymers[43,44] and multi-functional magnetic materials with conductivity,[45–47] fluorescence[48–50] and redox ability.[51–53]

In this study, we synthesized a novel homonuclear diiron(II) complex $[\{Fe(TPA)\}_2(\mu\text{-dto})](ClO_4)_2$ (**1**). When both Fe^{2+} centres have the same or different spin states, the dto bridging mode corresponds to a symmetric or asymmetric configuration, respectively. Notably, our spectroscopic and physical investigations revealed that **1** exhibits both symmetric and asymmetric dto bridging modes within the same crystal. This intriguing finding suggests the coexistence of different coordination fields, namely $\{N_4OS\}$, $\{N_4O_2\}$ and $\{N_4S_2\}$, around the Fe^{2+} centre. As a result of this unique situation, **1** exhibited a multi-step SCO and undergoes an irreversible structural and magnetic change at about 400 K. Our investigation aims to determine the relative proportions of symmetric and asym-

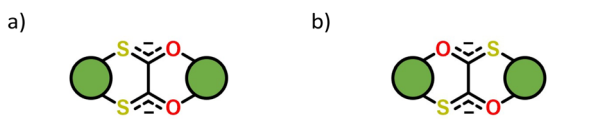

Fig. 1 Linkage isomers: (a) asymmetric and (b) symmetric conformations. Green filled circles represent metal centres.

[a]*Tokyo University of Science, 1-3 Kagurazaka, Shinjuku-ku, Tokyo 162-8601, Japan. E-mail: kanetomo@rs.tus.ac.jp, enomoto.masaya@rs.tus.ac.jp*
[b]*Waseda University, 3-4-1 Okubo, Shinjuku-ku, Tokyo 169-8555, Japan*

† Electronic supplementary information (ESI) available. CCDC 2108397–2108401. For ESI and crystallographic data in CIF or other electronic format see DOI: https://doi.org/10.1039/d3dt01992f

This journal is © The Royal Society of Chemistry 2023

Open Access Article. Published on 11 August 2023. Downloaded on 3/9/2026 9:36:11 AM.
This article is licensed under a Creative Commons Attribution-NonCommercial 3.0 Unported Licence.

metric dto bridging modes within **1** and to understand the factors that influence these distributions. In addition, we aim to gain insight into the mechanisms governing the magnetic properties exhibited by the compound.

Results and discussion

Synthesis and characterization

The dto-bridged diiron(II) complex **1** was prepared as green block crystals from $Fe^{II}(ClO_4)_2{\cdot}6H_2O$ (1 eq.), TPA (1 eq.), potassium dithiooxalate (0.5 eq.) and a small amount of ascorbic acid in methanol. The product was characterized by elemental analysis, mass spectroscopy and X-ray crystallographic analysis. The charge and spin states of the iron centres were determined by ^{57}Mössbauer spectroscopy (for details, see below). The thermal properties of **1** were evaluated by thermogravimetric analysis (TGA) and differential thermal analysis (DTA). The experimental curves, shown in Fig. 2, demonstrate that **1** exhibits a thermal stability of up to 440 K and does not contain any crystal solvents.

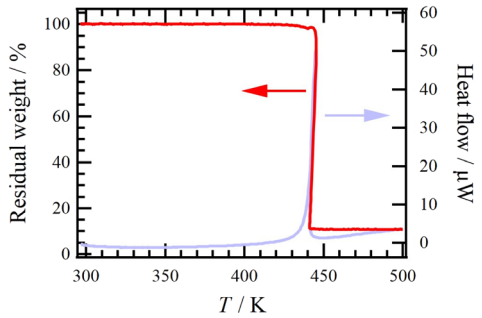

Fig. 2 TG (red line) and DTA curves (blue line) of **1**. The sweep rate of temperature is 2 K min^{-1}.

Crystal structure

Crystal structures of **1** were obtained at five different temperatures: initial 90, 293, 400, 223 and final 90 K. The corresponding crystallographic parameters are summarized in Table 1. Here, we describe the structure at an initial temperature of 90 K, while the temperature dependence of structural parameters will be discussed later. Compound **1** crystallizes in the monoclinic $P2_1/c$ space group. The asymmetric unit consists of the Fe^{2+} ion, the TPA capping ligand, half of the dto bridging ligand and the perchlorate anion. The centrosymmetric dinuclear complex comprises two Fe^{2+} centres with TPA bridged by dto shown in Fig. 3a. During the structural solution process, a non-negligible residual negative electron density was observed in the vicinity of the S1 atom. To solve this issue, it was necessary to consider a disordered state

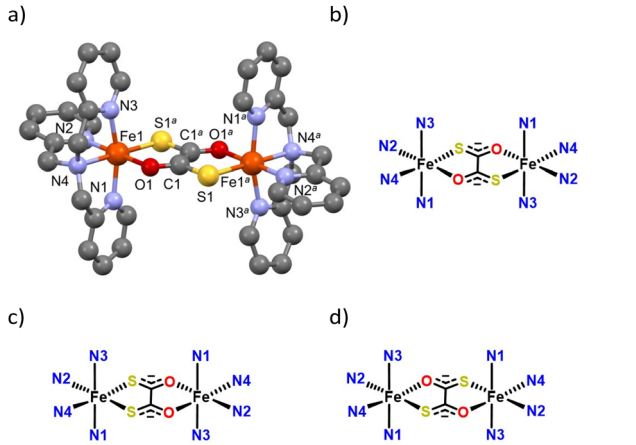

Fig. 3 (a) Crystal structure of **1** at 90 K (1st). Symmetric code: $a = 1 - x, -y, 1 - z$. The perchlorate anion molecules and H atoms are omitted for clarity. (b–d) Schematic isomers of dto in **1**. (b) **1-SymA**, (c) **1-Asym** and (d) **1-SymB**.

Table 1 Selected crystallographic parameters of **1**

T/K	90 (1st)	293	400	223	90 (2nd)
Formula	$C_{38}H_{36}Cl_2Fe_2N_8O_{10}S_2$				
Formula weight	1011.47				
Crystal system	Monoclinic				
Space group	$P2_1/c$				
a/Å	9.3104(10)	9.4639(6)	9.5293(15)	9.4258(9)	9.2720(18)
b/Å	13.5947(15)	13.8477(10)	13.955(2)	13.8090(15)	13.600(3)
c/Å	16.6268(17)	16.8880(11)	17.003(3)	16.7478(16)	16.515(3)
β/°	102.270(3)	104.177(2)	104.716(4)	104.095(3)	101.876(6)
V/Å^3	2056.4(4)	2145.8(2)	2187.0(6)	2114.3(4)	2037.9(7)
Z	2	2	2	2	2
d_{calcd}/g cm^{-3}	1.634	1.565	1.536	1.589	1.648
μ(Mo Kα)/mm^{-1}	1.006	0.964	0.946	0.978	1.015
$R(F)^a$ ($I > 2\sigma(I)$)	0.0658	0.0506	0.0566	0.0523	0.0563
$R_w(F_2)^b$ (all data)	0.1372	0.1252	0.1490	0.1401	0.1279
Goodness of fit	1.103	1.081	1.051	1.056	1.043
No. of unique reflns	4329	3262	3402	4706	4438
Occupancy factor (p_1)	0.672(9)	0.668(8)	0.748(9)	0.765(7)	0.728(9)

$^a R = \sum||F_o| - |F_c||/\sum|F_o|$. $^b R_w = [\sum w|F_o^2 - F_c^2|^2/\sum w(F_o^2)^2]^{1/2}$.

Open Access Article. Published on 11 August 2023. Downloaded on 3/9/2026 9:36:11 AM.
This article is licensed under a Creative Commons Attribution-NonCommercial 3.0 Unported Licence.

associated with different coordination forms, **1-SymA**, **1-Asym** (linkage isomer) and **1-SymB** (diastereomer), as illustrated in Fig. 3b–d. Note that **1-SymA** means that the N4 atom is positioned opposite to the S atom, whereas the diastereomer (**1-SymB**) means that the N4 atom is positioned opposite to the O atom. However, the simultaneous analysis of three isomers in the disorder model posed a significant challenge. To overcome this difficulty, we employed a mixed occupancy model, which is used in the analysis of inorganic compounds.[54,55] This model assumes that the S1 and O1 sites have mixed occupancy by the S1/O2 and O1/S2 atoms, respectively, with occupancy factors denoted as p_1 and p_2 (where $p_1 + p_2 = 1$). The analysis revealed that at an initial temperature of 90 K, the p_1 and p_2 factors were determined to be 0.672(9) and 0.328(9), respectively. Furthermore, the estimated ratios of the isomers **1-SymA**, **1-SymB** and **1-Asym** were found to be 0.45(1), 0.108(6) and 0.44(2), respectively.‡ Four Fe–N distances (Fe1–N1 to Fe1–N4) are 1.993(3)–2.060(4) Å, which are close to the typical values observed for the *ls*-Fe^{2+} ion (1.95–2.00 Å).[28]

The selected structural parameters of the dto moiety are summarized in Table 2. The C1–C1, C1–O1/S2 and C1–S1/O2 bond lengths are 1.520(7), 1.324(6) and 1.582(5) Å, respectively. Compared to the mean of the reported values for the C–C, C–O and C–S bond lengths (1.53(3), 1.24(4) and 1.70(4) Å, respectively),[1,10,13–17,25–27] the values in this work show only a negligible difference in the C–C bond length. However, the experimental C–O bond length is longer than the referential value, while the experimental C–S bond length is shorter. These findings suggest that the values of C1–O1 and C1–S1 are influenced by the presence of C1–S2 and C1–O2 bonds, respectively.

Both intramolecular and intermolecular interactions between the dto and TPA ligands were observed in the crystal structure, as shown in Fig. 4. First, the intramolecular distance S1/O2···C8 is 3.209(5) Å, while the O1/S2···C7 and O1/S2···C19 distances are 3.159(6) and 3.262(5) Å, respectively (green dashed lines in Fig. 4). These values are smaller or comparable to the sum of the van der Waals (vdW) radii (C/S: 3.50 Å; C/O: 3.22 Å),[56] even considering the influence of the disordered analysis. On the other hand, the intermolecular distances of O1/S2···C11, O1/S2···C5, S1/O2···C11 and S1/O2···C5 are 3.391(6), 3.443(5), 3.534(6) and 3.714(5) Å, respectively (blue dashed lines in Fig. 4). Although these values were found to be slightly larger than the sum of the vdW radii, it is important to consider the actual positions of the O and S atoms in dto. These positions may allow the formation of intermolecular contacts. The ClO_4 anions are located surrounding the $[\{Fe^{II}(TPA)\}_2(\mu\text{-dto})]$ cation units, resulting in the anions being sufficiently isolated from each other.

‡The ratios of the isomers **1-symA**, **1-symB** and **1-Asym** were determined using the formulas, $p_1 \times p_1$, $(1 - p_1) \times (1 - p_1)$ and $2 \times \{p_1 \times (1 - p_1)\}$, respectively, where p_1 represents the occupancy factor of the predominant atoms (O1 and S1); for example, a p_1 value of 0.672(9) at an initial temperature of 90 K gives 0.672 × 0.672, 0.328 × 0.328 and 2 × (0.672 × 0.328) for **1-SymA** (0.45(1)), **1-SymB** (0.108(6)) and **1-Asym** (0.44(2)), respectively.

Table 2 Selected crystallographic parameters of **1** at 90 (1st), 293, 400, 223 and 90 (2nd) K

T/K	90 (1st)	293	400	223	90 (2nd)
Coordination bond length					
Fe1–N1/Å	2.015(4)	2.121(4)	2.153(4)	2.114(3)	2.017(3)
Fe1–N2/Å	1.993(3)	2.110(3)	2.138(3)	2.097(3)	1.993(3)
Fe1–N3/Å	2.017(3)	2.130(4)	2.169(4)	2.126(3)	2.025(3)
Fe1–N4/Å	2.060(4)	2.192(3)	2.232(4)	2.185(3)	2.061(3)
Fe1–O1/Å	2.101(3)	2.175(3)	2.174(3)	2.131(2)	2.036(3)
Fe1–S1/Å	2.296(2)	2.287(2)	2.368(2)	2.330(1)	2.311(2)
Bond length in the dto ligand					
C1–C1[a]/Å	1.520(7)	1.528(8)	1.540(6)	1.522(5)	1.516(6)
C1–O1/Å	1.324(6)	1.351(5)	1.246(6)	1.258(5)	1.272(6)
C1–S1/Å	1.582(5)	1.585(4)	1.634(5)	1.635(2)	1.624(4)
Intra- and intermolecular distances					
S1···C8[a]/Å	3.209(5)	3.414(5)	3.531(6)	3.439(4)	3.244(4)
O1···C7/Å	3.159(6)	3.353(6)	3.442(8)	3.353(5)	3.146(6)
O1···C19/Å	3.262(5)	3.471(6)	3.582(7)	3.469(5)	3.239(6)
S1···C5[b]/Å	3.714(5)	3.689(6)	3.643(7)	3.622(5)	3.656(5)
S1···C11[c]/Å	3.534(6)	3.550(6)	3.535(7)	3.493(4)	3.498(6)
O1···C5[b]/Å	3.443(5)	3.457(6)	3.569(8)	3.513(5)	3.535(5)
O1···C11[c]/Å	3.391(6)	3.373(6)	3.415(8)	3.358(5)	3.390(6)
O4···C16[d]/Å	3.078(7)	3.169(9)	3.22(1)	3.125(7)	3.063(6)

[a] 1 − *x*, −*y*, 1 − *z*. [b] 2 − *x*, −*y*, 1 − *z*. [c] *x*, −1/2 − *y*, 1/2 + *z*. [d] 1 − *x*, 1/2 + *y*, 1/2 − *z*.

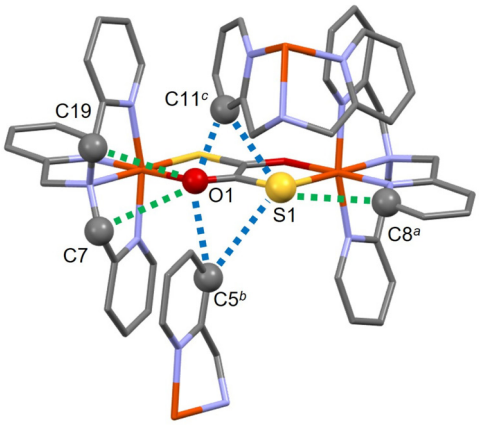

Fig. 4 Intra- and intermolecular hydrogen bonds of **1** at 1st 90 K. Symmetric code: *a* = 1 − *x*, −*y*, 1 − *z*; *b* = 2 − *x*, −*y*, 1 − *z*; and *c* = *x*, −1/2 − *y*, 1/2 + *z*. The perchlorate anions and H atoms are omitted for clarity. Green and blue dashed lines represent the intra- and intermolecular contacts, respectively.

Magnetic properties

The magnetic properties of the polycrystalline **1** were investigated through heating and cooling processes. During the first heating (5–400 K; red open circles in Fig. 5), the values exhibited a plateau at 0.6–0.9 cm^3 K mol^{-1} between 10 K and 100 K. These values were larger than the theoretical values expected for two *ls*-Fe^{2+} ions (S = 0; 0 cm^3 K mol^{-1}). The residual magnetic momentum indicated the presence of a small amount of *hs*-Fe^{2+}, which was confirmed by ^{57}Fe Mössbauer spectroscopy (for details, see below). Upon further heating from 100 K, the $\chi_m T$ values exhibited three-step SCO behaviours: 1st,

Open Access Article. Published on 11 August 2023. Downloaded on 3/9/2026 9:36:11 AM.
This article is licensed under a Creative Commons Attribution-NonCommercial 3.0 Unported Licence.

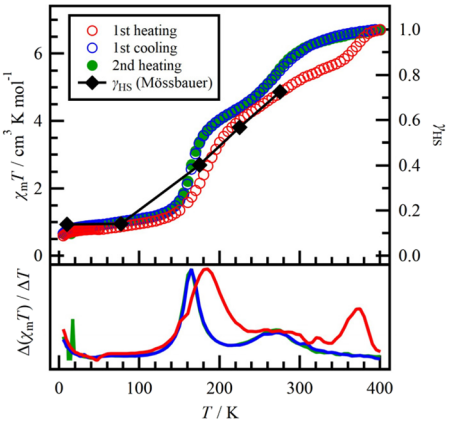

Fig. 5 Temperature dependence of the product $\chi_m T$ and the HS fraction γ_{HS} of **1** measured at 0.5 T. Black diamonds represent γ_{HS} of **1** obtained from the results of Mössbauer spectra (for details, see the text).

150–200 K; 2nd, 200–350 K; and 3rd, 350–400 K. In the $\Delta(\chi_m T)/\Delta T$ *vs.* T plot (Fig. 5), two distinct peaks corresponding to the abrupt 1st and 3rd SCO behaviours were observed, giving the transition temperatures T_{c1} = 184 K and T_{c3} = 371 K, respectively. Considering the presence of three isomers in **1** as shown in Fig. 3b–d, we must take into account four Fe^{2+} centres with different coordination fields: namely, two species of N_4OS (α and β) from **1-SymA** and **1-SymB**, respectively, and N_4O_2 and N_4S_2 from **1-Asym**. Comparing the energy levels and the magnitude of the orbital lobes for the O and S atoms, the coordination field for N_4O_2 is weaker than that of N_4S_2. Therefore, the 1st, 2nd and 3rd SCO behaviours can be attributed to α-N_4OS, β-N_4OS and N_4S_2, respectively, based on the order of coordination fields and the corresponding changes in $\chi_m T$ values. There could also be slight variation in the exact coordination field between **1-SymA** and **1-SymB**, leading to differences in the SCO temperature. After the 3rd SCO behaviour, the $\chi_m T$ value reached 6.71 cm^3 K mol^{-1} at 400 K. Although this value suggests that all iron(II) centres are in the *hs* state, it exceeds the expected value of 6.0 cm^3 K mol^{-1}, which is derived from two *hs*-Fe^{2+} ions (S = 2 and g = 2.0; 3.0 cm^3 K mol^{-1}). This discrepancy indicates that the g value is greater than 2, due to the distorted coordination environment around the *hs*-Fe^{2+} centres.[28]

During the cooling process from 400 K (blue open circles in Fig. 5), $\chi_m T$ showed a clear two-step SCO behaviour (1st, 100–200 K; 2nd, 200–300 K), compared to the 1st heating process. The $\Delta(\chi_m T)/\Delta T$ *vs.* T plot gave the transition temperatures T'_{c1} = 165 K and T'_{c2} = 268 K. The 1st SCO behaviour observed during the cooling process is comparable to that observed during the 1st heating process. However, the 2nd SCO behaviour appears to be a cooperative occurrence of the 2nd and 3rd SCO behaviours observed in the 1st heating process. When heated again from 5 K (2nd heating process, green filled circles in Fig. 5), the $\chi_m T$ values followed the same route as the cooling process. This observation indicates an irreversible change between the 1st heating and cooling processes. While the desorption of the crystalline solvent could be a potential cause of this irreversible change, such a scenario was ruled out by TGA and structural studies. In this study, we propose that the as-grown crystal of **1** is initially metastable and undergoes a transition to a stable state during the 1st heating process. The stable state could have a lower ΔH_{trs}, which is a transition enthalpy defined as $\Delta G = \Delta H_{trs} - T_c \Delta S_{trs} = 0$, compared to the metastable state due to the lowered transition temperatures after the irreversible change. The decrease in ΔH_{trs} is often explained by a change in the structural factor corresponding to the crystal lattice and the coordination field around the Fe^{2+} centres.

^{57}Fe Mössbauer spectroscopy

Variable temperature ^{57}Fe Mössbauer spectra were utilized to determine the spin state of the iron centres in **1**. The spectra were recorded during the 1st heating process and the results are presented in Table 3 and Fig. 6.

At 10 K, the Mössbauer spectrum exhibited three distinct doublets. The major doublet (blue filled area) showed a quadrupole splitting (ΔE_Q) of 0.574(2) mm s^{-1} and an isomer shift (δ) of 0.4669(10) mm s^{-1}, indicating the presence of Fe^{2+} atoms in the *ls* state (*ls*-A).[1] Two minor doublets (green and yellow areas) exhibited ΔE_Q and δ values of 1.92(2) and 1.327(10) mm s^{-1} and 2.97(2) and 1.063(8) mm s^{-1}, respectively. These minor doublets were assigned to *hs*-Fe^{2+} sites,[1] namely, *hs*-A (green area) and *hs*-B (yellow area).

Upon heating from 10 K to 275 K, the intensity of the *ls*-A doublet decreased to about 60% of the total area, while the *hs*-B signal increased (Table 3). This result provides evidence for the SCO behaviour of the Fe^{2+} centres, corresponding to the *ls* and *hs* states for α-N_4OS and a part of β-N_4OS, as discussed in the magnetic studies. In addition, the *hs*-A area remained almost constant across all temperatures and was utilized as the fixed parameter for analysis above 175 K. This temperature-independent component can be attributed to N_4O_2, which exhibits the weakest coordination field. Furthermore, the *ls*-A

Table 3 Mössbauer parameters of **1** at 10, 77, 175, 225 and 275 K

T/K	Spin state	Area/%	δ^a/mm s^{-1}	$\Delta E_Q{}^b$/mm s^{-1}	Γ^c/mm s^{-1}
10	*hs*-A	9.4	1.327(10)	1.92(2)	0.42(4)
	hs-B	4.5	1.063(8)	2.97(2)	0.24(3)
	ls-A	86.1	0.4669(10)	0.574(2)	0.399(3)
77	*hs*-A	9.5	1.32(2)	1.96(3)	0.51(6)
	hs-B	4.7	1.058(11)	3.01(2)	0.27(4)
	ls-A	85.8	0.462(1)	0.569(3)	0.444(4)
175	*hs*-A	9.5 (fixed)	1.155(10)	1.83(2)	0.32(2)
	hs-B	30.7	0.962(4)	2.958(8)	0.433(13)
	ls-A	59.8	0.411(2)	0.607(4)	0.413(7)
225	*hs*-A	9.5 (fixed)	1.084(11)	1.75(2)	0.31(2)
	hs-B	47.3	0.948(4)	2.821(9)	0.54(2)
	ls-A	43.2	0.392(5)	0.621(9)	0.46(2)
275	*hs*-A	9.5 (fixed)	0.87(2)	1.67(4)	0.34(4)
	hs-B	63.1	0.904(6)	2.600(12)	0.61(2)
	ls-A	27.4	0.341(2)	0.44(3)	0.58(6)

[a] δ [mm s^{-1}] = isomer shift. [b] ΔE_Q [mm s^{-1}] = quadrupole splitting. [c] Γ [mm s^{-1}] = full width at the half-maximum (FWHM) of the line.

Open Access Article. Published on 11 August 2023. Downloaded on 3/9/2026 9:36:11 AM.
This article is licensed under a Creative Commons Attribution-NonCommercial 3.0 Unported Licence.

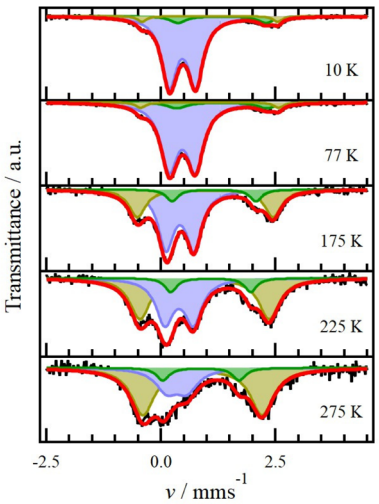

Fig. 6 ^{57}Fe Mössbauer spectra of **1** recorded at 10, 77, 175, 225 and 275 K. The blue pattern represents the area of ***ls*-A**, and the green and yellow patterns represent the areas of ***hs*-A** and ***hs*-B**, respectively.

component is attributed to the N_4S_2 environment, which has the same area as N_4O_2 (*hs*-A).

The sum of the areas of *hs*-A and *hs*-B at each temperature was superimposed as shown in Fig. 5. These data agree well with the fraction of the *hs* state (γ_{HS}) determined from the corresponding $\chi_m T$ values. Overall, the ^{57}Fe Mössbauer spectra directly support the SCO phenomenon at the Fe^{2+} sites in **1**.

Variable-temperature dependence of single-crystal X-ray diffraction

We performed variable-temperature single-crystal X-ray diffraction of **1** upon heating (90, 293 and 400 K) and then cooling (223 and 90 K), as shown in Table 1 and 2. Compound **1** exhibited in the monoclinic $P2_1/c$ space group at all temperatures. Fig. 7a shows the temperature dependence of the cell parameters, *a*, *b*, *c* and *V*. There was a slight difference in cell parameters (<1%) between the initial and final 90 K, indicating the irreversible structural change.

Fig. 7b shows the temperature dependence of the bond lengths in dto. Although there are negligible differences in the C–C bond lengths across all temperatures, the C–O and C–S bond lengths undergo noticeable changes from 293 K to 400 K. The occupancy value p_1 also increases from the initial 90 K (0.672) to the final 90 K (0.728).

At the initial 90 K, the four Fe–N distances indicate the *ls* state of the Fe^{2+} centre. Upon heating to 293 K, these lengths increase and fall within the typical range of 2.12–2.18 Å observed for *hs*-Fe^{2+} complexes.[28] These structural changes are consistent with the SCO behaviour of the Fe^{2+} centres. Fig. 7c shows that the Fe1–O1 bond length decreases while the Fe1–S1 one increases, between the initial and final 90 K. These findings suggest potential strengthening or weakening, respectively, of the coordination field around the Fe^{2+} centre. Based on the magnetic studies conducted, it is hypothesized that the change in the Fe–S bond plays a dominant role and contributes to a lower SCO temperature during the cooling process compared to the 1st heating process.

The temperature dependence of intramolecular contacts between dto and TPA moieties is shown in Fig. 7d. At the initial 90 K, the O1/S2···C7, O1/S2···C19 and S1/O2···C8 distances are 3.159(6), 3.262(5) and 3.209(5) Å, respectively. Upon heating to 400 K, these distances increased to 3.442(8), 3.582(7) and 3.531(6) Å, respectively, which are larger than the sum of vdW radii (C/S: 3.50 Å; C/O: 3.22 Å).[56] This change in intramolecular distances indicates the weakening of the contacts

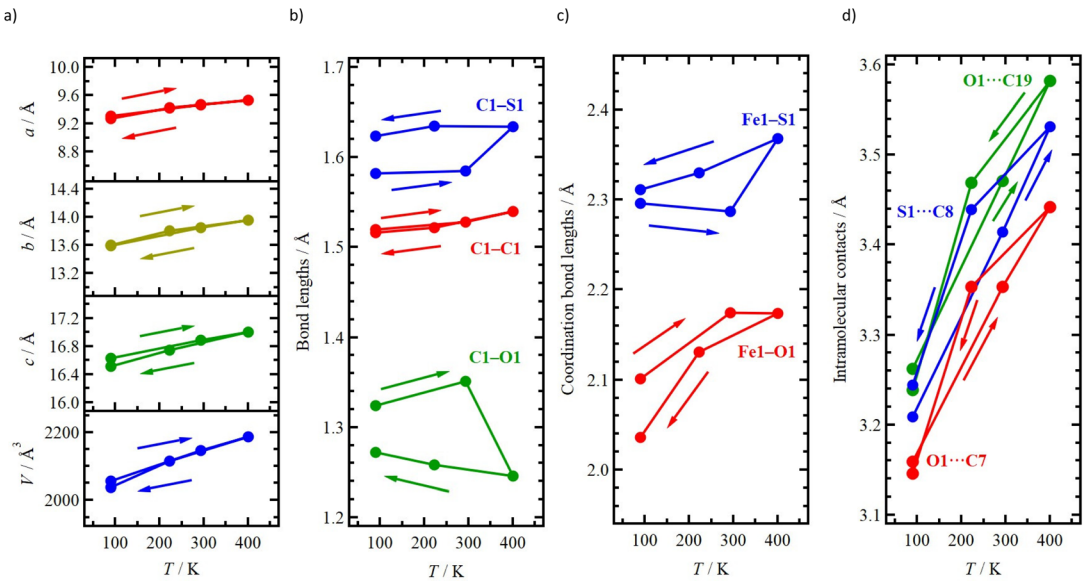

Fig. 7 Temperature dependence of selected structural parameters. (a) Cell parameters: *a* (red), *b* (yellow), *c* (green) and *V* (blue). (b) Bond lengths in the dto moiety; C1–C1 (red), C1–O1 (green) and C1–S1 (blue). (c) Coordination bonds around the Fe^{2+} centre: Fe1–O1 (red) and Fe1–S1 (blue). (d) Intramolecular contacts: O1···C7 (red), O1···C19 (green) and S1···C8 (blue). The arrows represent the direction of the temperature sweep.

Open Access Article. Published on 11 August 2023. Downloaded on 3/9/2026 9:36:11 AM.
This article is licensed under a Creative Commons Attribution-NonCommercial 3.0 Unported Licence.

between the dto and TPA moieties, leading to increased freedom of motion for dto. As a result of this increased freedom, **1** exhibits an irreversible change from metastable to stable phases. It is likely that the formation of the metastable phase is related to the synthetic conditions during the mixing of the three isomers (Fig. 3). Before the crystallization of **1**, the reaction solution was held at 300 K (reaction) and 255 K (crystallization). Based on magnetic studies conducted in the solid state (Fig. 5), **1** exhibits SCO behaviour. It is important to note that the transition temperature in solution can be lower than that in the solid state due to a reduction in ΔH_{trs}. This lower T_c in solution allows **1** to exist as a mixture of *hs* and *ls* states. In this particular condition, the bridging conformation of the dto ligand could be confused with either the symmetric or asymmetric form. This conformation confusion leads to incomplete crystallization, resulting in the formation of a metastable phase.

Conclusions

We have synthesized a novel dto-bridged diiron(II) complex **1**. The bridging ligand (dto) adopts a symmetric *S*,*O*-chelation form, while **1** also encompasses the linkage isomer (*S*,*S*- and *O*,*O*-chelation) and the diastereomer within the same crystal. The bridging modes of dto in **1** are influenced by the spin state (*hs* or *ls*) of the two Fe^{2+} centres. During complex formation, the modes are determined by the Fe centres, resulting in a mixture of the three isomeric forms due to the presence of both *hs* and *ls* states. These isomers exhibit distinct temperature-dependent magnetic properties, and **1** displays a multistep SCO behaviour. Interestingly, magnetic studies revealed differences in SCO behaviour between the first heating and cooling processes. This discrepancy can be attributed to an irreversible structural change occurring within the complex. Our observations indicate that the transition from the metastable phase to the stable phase is triggered by the thermal expansion of the crystal and the stretching of bond lengths due to the SCO phenomenon.

Experimental

Materials and methods

Iron(II) perchlorate hexahydrate, TPA, ascorbic acid and methanol were purchased. Methanol was used as the solvent without further purification. Potassium 1,2-dithiooxalate K_2(dto) was prepared using the previously reported procedure.[57] Infrared (IR) spectra were recorded using a JASCO FT/IR-4600 spectrometer by the diamond attenuated total reflectance (ATR) method. The spectral data were reported in the form of major peaks in wavenumbers (cm^{-1}). The peaks were recorded in a spectral window of 4000–400 cm^{-1}. Elemental analyses were carried out using a PerkinElmer Series II CHNS/O 2400 analyser. Thermogravimetry and differential thermal analysis (TG and DTA, respectively) of **1** were carried out using a Bruker AXS TG2000SA. The temperature scan rate was 2 K min^{-1} in the range of 296–481 K. Melting point measurement was performed using an ATM-02 (AS ONE). Mass spectra (MS) were recorded in the electrospray ionization (ESI) mode using an AccuTOF-JMS-T100LP (JEOL) spectrometer. The specimen was dissolved in methanol.

Synthesis of $[\{Fe(TPA)\}_2(\mu\text{-dto})](ClO_4)_2$ (1)

Under an Ar atmosphere, iron(II) perchlorate hexahydrate (51.0 mg, 0.141 mmol), TPA (43.1 mg, 0.148 mmol) and ascorbic acid (7.9 mg) were dissolved in methanol (30 mL). K_2(dto) powder (8.30 mg, 0.0420 mmol) was added to the solution. The reaction mixture was stored in a refrigerator (<−18 °C). The precipitated polycrystals were separated on a filter and washed with distilled water. The yield of **1** was 13.1 mg (0.0130 mmol, 31%). Melting point: 185 °C (dec.). Analytical calculations for $C_{38}H_{36}N_8S_2O_{10}Fe_2Cl_2$: C, 45.12; H, 3.59; N, 11.08%. Result: C, 44.77; H, 3.37; N, 10.81%. IR (ATR): 1530, 1478, 1439, 1075, 1053, 1020, 870, 763, 620 and 596 cm^{-1}. MS (ESI+): *m*/*z* 911.2 and 913.2 [**1**-ClO_4].

Single crystal X-ray diffraction (SXRD)

X-ray diffraction data of **1** were collected on a Bruker D8 Quest diffractometer (Mo Kα radiation: λ = 0.71073 Å). X-ray data analysis was carried out using SHELXT[58] and SHELXL,[59] which were operated with Olex2 software.[60] Numerical absorption correction was used. All hydrogen atoms were refined using the riding model. The thermal displacement parameters of the nonhydrogen atoms were refined anisotropically. The Cambridge Crystallographic Data Centre (CCDC) numbers of **1** are 2108397–2108401† measured at 90 (1st), 90 (2nd), 223, 400 and 293 K, respectively.

Magnetic measurements

The direct current magnetic properties of the polycrystalline specimens of **1** in wrap were measured using a Quantum Design MPMS-XL7AC SQUID magnetometer equipped with a 7 T coil in the temperature range of 5–400 K. The experimental data were corrected using the measured diamagnetic blank data of the sample holder. The diamagnetic contribution of the sample was estimated using Pascal's constants.[61]

Mössbauer spectroscopy

^{57}Fe Mössbauer spectra of **1** were recorded on a constant acceleration spectrometer with a γ-ray source of ^{57}Co/Rh in the transmission mode. The measurements were performed using a closed-cycle helium refrigerator (Iwatani Industrial Gases Corp.) and a conventional Mössbauer spectrometer (Topologic Systems). All isomer shifts were obtained relative to α-Fe at room temperature. The Mössbauer spectra were fitted using the least-squares fitting program MossWinn 4.0.[62]

Conflicts of interest

There are no conflicts to declare.

Open Access Article. Published on 11 August 2023. Downloaded on 3/9/2026 9:36:11 AM.
This article is licensed under a Creative Commons Attribution-NonCommercial 3.0 Unported Licence.

Acknowledgements

The structural solution of **1** was prepared as advised by Prof. Nobuyuki Matsushita at Rikkyo University, Japan. Mr Daigo Matsunaga and Ms Sayaka Ono (Tokyo University of Science) collected the MS data for **1**.

Notes and references

1 W. Dietzsch, P. Strauch and E. Hoyer, *Coord. Chem. Rev.*, 1992, **121**, 43.
2 M. Mitsumi, H. Okawa, H. Sakiyama, M. Ohba, N. Matsumoto, T. Kurisaki and H. Wakita, *J. Chem. Soc., Dalton Trans.*, 1993, 2991.
3 S. Decurtins, H. W. Schmalle, R. Pellaux, P. Schneuwly and A. Hauser, *Inorg. Chem.*, 1996, **35**, 1451.
4 M. Siebold, S. Eidner, A. Kelling, M. U. Kumke, U. Schilde and P. Strauch, *Z. Anorg. Allg. Chem.*, 2006, **632**, 1963.
5 M. Nowotny, S. Foro, S. Heinschke, R. C. Hoffmann and J. J. Schneider, *Eur. J. Inorg. Chem.*, 2015, 512.
6 J. König, A. Kelling, U. Schilde and P. Strauch, *Molbank*, 2016, **2016**, M895.
7 A. Hijazi, J. C. Kemmegne-Mbouguen, S. Floquet, J. Marrot, C. R. Mayer, V. Artero and E. Cadot, *Inorg. Chem.*, 2011, **50**, 9031.
8 J. McGuire, B. Wilson, J. McAllister, H. N. Miras, C. Wilson, S. Sproules and J. H. Farnaby, *Dalton Trans.*, 2019, **48**, 5491.
9 M. Nakayama, T. Kanetomo and M. Enomoto, *Chem. Lett.*, 2020, **49**, 1050.
10 C. J. Adams, *J. Chem. Soc., Dalton Trans.*, 2002, 1545.
11 H. Ōkawa, M. Mitsumi, M. Ohba, M. Kodera and N. Matsumoto, *Bull. Chem. Soc. Jpn.*, 1994, **67**, 2139.
12 J. M. Bradley, S. G. Carling, D. Visser, P. Day, D. Hautot and G. J. Long, *Inorg. Chem.*, 2003, **42**, 986.
13 Y. Ono, M. Okubo and N. Kojima, *Solid State Commun.*, 2003, **126**, 291.
14 G.-F. Xu, P. Gamez, J. Tang, R. Clérac, Y.-N. Guo and Y. Guo, *Inorg. Chem.*, 2012, **51**, 5693.
15 M. Itoi, Y. Ono, N. Kojima, K. Kato, K. Osaka and M. Takata, *Eur. J. Inorg. Chem.*, 2006, 1198.
16 M. Itoi, A. Okazawa, J. Yamaura, S. Maki, T. Komatsu, I. Maurin, E. Codjovi, K. Boukheddaden and N. Kojima, *Inorg. Chem.*, 2018, **57**, 13728.
17 K. Nomura, T. Kanetomo and M. Enomoto, *Cryst. Growth Des.*, 2022, **22**, 2139.
18 T. Nakamoto, Y. Miyazaki, M. Itoi, Y. Ono, N. Kojima and M. Sorai, *Angew. Chem., Int. Ed.*, 2001, **40**, 4716.
19 Y. Kobayashi, M. Itoi, N. Kojima and K. Asai, *J. Phys. Soc. Jpn.*, 2002, **71**, 3016.
20 N. Kida, M. Enomoto, I. Watanabe, T. Suzuki and N. Kojima, *Phys. Rev. B: Condens. Matter Mater. Phys.*, 2008, **77**, 144427.
21 N. Kida, M. Hikita, I. Kashima, M. Okubo, M. Itoi, M. Enomoto, K. Kato, M. Takata and N. Kojima, *J. Am. Chem. Soc.*, 2009, **131**, 212.
22 X. Liu, B. Wang, X. Huang, X. Dong, Y. Ren, H. Zhao, L. Long and L. Zheng, *J. Am. Chem. Soc.*, 2021, **143**, 5779.
23 P. D. W. Boyd, J. Hope, C. L. Raston and A. H. White, *Aust. J. Chem.*, 1990, **43**, 601.
24 D. Coucouvanis and D. Piltingsrud, *J. Am. Chem. Soc.*, 1973, **95**, 5556.
25 L. Golič, N. Bulc and W. Dietzsch, *Inorg. Chem.*, 1982, **21**, 3560.
26 L. Golič, N. Bulc and W. Dietzsch, *Polyhedron*, 1983, **2**, 1201.
27 C. A. Hester, M. Draganjac and A. W. Cordes, *Inorg. Chim. Acta*, 1991, **184**, 137.
28 *Spin Crossover in Transition Metal Compounds I, II, and III*, ed. P. Gütlich and H. A. Goodwin, Springer, Berlin, 2004.
29 P. Gütlich, Y. Garcia and H. A. Goodwin, *Chem. Soc. Rev.*, 2000, **29**, 419.
30 R. W. Hogue, S. Singh and S. Brooker, *Chem. Soc. Rev.*, 2018, **47**, 7303.
31 H. Hagiwara, R. Minoura, T. Udagawa, K. Mibu and J. Okabayashi, *Inorg. Chem.*, 2020, **59**, 9866.
32 M. J. H. Ojea, J. M. van Raden, S. Louie, R. Collins, D. Pividori, J. Cirera, K. Meyer, R. Jasti and R. A. Layfield, *Angew. Chem., Int. Ed.*, 2021, **60**, 3515.
33 S. Mossin, B. L. Tran, D. Adhikari, M. Pink, F. W. Heinemann, J. Sutter, R. K. Szilagyi, K. Meyer and D. J. A. Mindiola, *J. Am. Chem. Soc.*, 2012, **134**, 13651.
34 Z.-Y. Li, H. Ohtsu, T. Kojima, J.-W. Dai, T. Yoshida, B. K. Breedlove, W.-X. Zhang, H. Iguchi, O. Sato, M. Kawano and M. Yamashita, *Angew. Chem., Int. Ed.*, 2016, **55**, 5184.
35 S. K. Karuppannan, A. Martín-Rodríguez, E. Ruiz, P. Harding, D. J. Harding, X. Yu, A. Tadich, B. Cowie, D. Qi and C. A. Nijhuis, *Chem. Sci.*, 2021, **12**, 2381.
36 S. Hayami, Y. Komatsu, T. Shimizu, H. Kamihata and Y. H. Lee, *Coord. Chem. Rev.*, 2011, **255**, 1981.
37 O. Drath and C. Boskovic, *Coord. Chem. Rev.*, 2018, **375**, 256.
38 S. Ghosh, S. Selvamani, S. Mehta and A. Mondal, *Dalton Trans.*, 2020, **49**, 9208.
39 R. Akiyoshi, Y. Komatsumaru, M. Donoshita, S. Dekura, Y. Yoshida, H. Kitagawa, Y. Kitagawa, L. F. Lindoy and S. Hayami, *Angew. Chem., Int. Ed.*, 2021, **60**, 12717.
40 T. Kanetomo, Z. Ni and M. Enomoto, *Dalton Trans.*, 2022, **51**, 3034.
41 G. G. Morgan, K. D. Murnaghan, H. Müller-Bunz, V. McKee and C. J. A. Harding, *Angew. Chem., Int. Ed.*, 2006, **45**, 7192.
42 S. Wang, M. Ferbinteanu, C. Marinescu, A. Dobrinescu, Q.-D. Ling and W. Huang, *Inorg. Chem.*, 2010, **49**, 9839.
43 *Molecular Magnetic Materials*, ed. B. Sieklucka and D. Pinkowich, Wiley-VCH, Weinheim, 2017.
44 F. Bigdeli, C. T. Lollar, A. Morsali and H.-C. Zhou, *Angew. Chem., Int. Ed.*, 2020, **59**, 4652.
45 K. Takahashi, H.-B. Cui, Y. Okano, H. Kobayashi, H. Mori, H. Tajima, Y. Einaga and O. Sato, *J. Am. Chem. Soc.*, 2008, **130**, 6688.
46 H. Phan, S. M. Benjamin, E. Steven, J. S. Brooks and M. Shatruk, *Angew. Chem.*, 2015, **127**, 837.

 This journal is © The Royal Society of Chemistry 2023

Open Access Article. Published on 11 August 2023. Downloaded on 3/9/2026 9:36:11 AM.
This article is licensed under a Creative Commons Attribution-NonCommercial 3.0 Unported Licence.

47 R. Ishikawa, S. Ueno, S. Nifuku, Y. Horii, H. Iguchi, Y. Miyazaki, M. Nakano, S. Hayami, S. Kumagai, K. Katoh, Z.-Y. Li, M. Yamashita and S. Kawata, *Chem. – Eur. J.*, 2020, **26**, 1278.
48 J. Yuan, S.-Q. Wu, M.-J. Liu, O. Sato and H.-Z. Kou, *J. Am. Chem. Soc.*, 2018, **140**, 9426.
49 C.-F. Wang, G.-Y. Yang, Z.-S. Yao and J. Tao, *Chem. – Eur. J.*, 2018, **24**, 3218.
50 S. Ghosh, S. Kamilya, T. Pramanik, M. Rouzières, R. Herchel, S. Mehta and A. Mondal, *Inorg. Chem.*, 2020, **59**, 13009.
51 B. Schneider, S. Demeshko, S. Dechert and F. Meyer, *Angew. Chem., Int. Ed.*, 2010, **49**, 9274.
52 I. A. Gural'skiy, S. I. Shylin, V. Ksenofontov and W. Tremel, *Eur. J. Inorg. Chem.*, 2017, 3125.
53 L. Zappe, S. Schönfeld, G. Hörner, K. A. Zenere, C. F. Leong, C. J. Kepert, D. M. D'Alessandro, B. Weber and S. M. Neville, *Chem. Commun.*, 2020, **56**, 10469.
54 K. Mereiter, *Acta Crystallogr., Sect. C: Cryst. Struct. Commun.*, 2013, **69**, 1085.
55 S. Funahashi, Y. Michiue, T. Takeda, R.-J. Xie and N. Hirosaki, *Acta Crystallogr., Sect. C: Struct. Chem.*, 2014, **70**, 452.
56 A. Bondi, *J. Phys. Chem.*, 1964, **68**, 441.
57 H. S. Tasker and H. O. Jones, *J. Chem. Soc., Trans.*, 1909, **95**, 1910.
58 G. M. Sheldrick, *Acta Crystallogr., Sect. A: Found. Adv.*, 2015, **71**, 3.
59 G. M. Sheldrick, *Acta Crystallogr., Sect. C: Struct. Chem.*, 2015, **71**, 3.
60 L. J. Bourhis, O. V. Dolomanov, R. J. Gildea, J. A. K. Howard and H. Puschmann, *Acta Crystallogr., Sect. A: Found. Adv.*, 2015, **71**, 59.
61 O. Kahn, *Molecular Magnetism*, VCH-Verlag, Weinheim, New York, 1993.
62 Z. Klencsár, E. Kuzmann and A. Vértes, *J. Radioanal. Nucl. Chem.*, 1996, **210**, 105–118.